Towards superconducting spintronics with RuO2 and CrO2 nanowires

Prateek, K.

5

Fabrication and Properties of Lateral Josephson Junctions with a RuO_2 Weak Link

Ruthenium dioxide (RuO_2) is a metallic rutile oxide with a number of interesting properties. For a long time, it was considered to be a highly conductive normal metal and a Pauli paramagnet. Recently, it was found that the material is antiferromagnetic, with small magnetic moments of the order of 0.05 Bohr magneton and an ordering temperature above 300 K. The presence of magnetic moments should have clear consequences when trying to induce superconductivity in RuO_2. We used a selective area chemical vapor deposition method to grow nanowires of RuO_2 on TiO_2 substrates. On these wires, superconducting contacts were made of MoGe, and a weak link was fabricated with a Focused Ion Beam. We find that the device behaves as a Josephson junction, including a Fraunhofer-like response to a magnetic field, for distances between the contacts below 70 nm. We estimate the induced singlet coherence length ξ to be about 12 nm, which seems a reasonable number when small magnetic moments are present.

An adapted version of this chapter has been submitted for publication in a peer-reviewed journal as K. Prateek, T. Mechielsen, A.B. Hamida, D. Scholma and J. Aarts, *Fabrication and properties of lateral Josephson junctions with a RuO_2 weak link.*

5.1. Introduction

In recent years, there has been a revival of interest in the properties of the metallic rutile oxides CrO_2, RuO_2 and IrO_2, mainly in connection with magnetism, non-trivial Fermi surfaces, and possible spintronics applications [1, 2]. CrO_2 is a half-metallic ferromagnet that in bulk form was long used in magnetic tapes [3] and in thin film form was found of particular interest to study superconducting long rang range proximity effects [4–6]. IrO_2 was researched from a spintronics perspective as a material with large spin-orbit coupling [7, 8]. RuO_2 was long thought to be a normal metal, and in film form often used in low-temperature thermometry, because of ease of use and insensitivity of the resistance to even high magnetic fields. However, in 2017 itinerant antiferromagnetism was discovered [9], with magnetic moments of the order of 0.05 μ_B (with μ_B the Bohr magneton) and a (Néel) ordering temperature above 300 K. This was confirmed in another study [10], and also prompted renewed studies of the anomalous Hall effect [11, 12]. On the other hand, also superconductivity was recently reported in slightly strained films of RuO_2 [13].

Long range proximity effect has been recently observed in Mn_3Ge, resulting from the chiral non-collinear antiferromagnetic spin structure that creates a non-zero Berry phase [14]. The same study also reported that IrMn, a collinear antiferromagnet with moments on the Mn site of the order of 3 μ_B (Bohr magneton) [15], only shows short range supercurrents owing to its trivial topological spin arrangement. RuO_2, although also a collinear antiferromagnet, has been shown to have crystal inversion asymmetry arising from spin-splitting and time-reversal symmetry breaking in the band structure [16–18]. RuO_2 has also been identified as a promising candidate to allow for spin polarized currents which has been substantiated by recent transport measurements conducted on RuO_2 [19–21]. In this work, we investigate the proximity effect in RuO_2 nanowires by fabricating lateral Josephson junctions, using superconducting amorphous MoGe as electrodes. Since the resistivity of RuO_2 is quite low, we can expect a quite long induced coherence length if the material behaves as a normal metal. Instead, and confirming the presence of (small) magnetic moments, we find a short decay length (ξ) of around 12 nm which indicates the presence of only short range singlet Cooper pairs and absence of long range spin triplets. The chapter is organized in the following manner. We begin by examining the nanofabrication process that leads to Selective Area (SA)-grown nanowires. Subsequently, we proceed to characterize these RuO_2 nanowires through electrical and magneto-transport measurements. Then we focus on making Josephson junctions (JJ) in which superconducting MoGe are contacted on top of RuO_2 nanowires with varying lateral gaps and present the results on these junctions.

5.2. Selective area growth of RuO_2 nanowires

We grow RuO_2 nanowires on (100) oriented TiO_2 substrates using the same selective area growth technique as CrO_2 nanowires [22] since the lattice parameters of TiO_2, RuO_2 and CrO_2 are comparable and they all crystallize with a rutile structure and a tetragonal unit cell. RuO_2 has the attice parameters a = b = 0.4499 nm and c = 0.3107 nm while TiO_2 has the values of a = b = 0.4594 nm and c = 0.2958 nm. Compared to the TiO_2 lattice, the [010] and [001] directions of bulk RuO_2 have a lattice mismatch of approximately -2.1 % and +5.0 % respectively. Thus, RuO_2 thin films experience tensile strain along [010] while compressive strain along [001].

The fabrication of the RuO_2 nanowire starts with an HF etch of TiO_2 substrate. This is then followed by depositing a SiO_x layer, which in our case has a thickness of approximately 25 nm, and electron beam patterning to create a positive resist mask with the desired device structure. Subsequently, the trench is selectively etched using reactive ion etching (RIE). We have observed that both underetching and overetching the trench is detrimental for a successful growth, similar to the case of CrO_2. RuO_2 nanowires are subsequently grown in the trenches using Chemical Vapor Deposition (CVD) in a two-zone furnace. During this process, the substrate temperature is maintained at 390°C while the precursor $(C_5H_5)_2Ru$ is heated to 80°C in the presence of an O_2 carrier gas flow. Fig. 5.1(a) shows the SEM image of an epitaxially grown RuO_2 nanowire along the [001] direction. RuO_2 also grows on the surface of SiO_x [23] albeit much more slowly than on TiO_2 which helps to prevent merging of small crystals of RuO_2 of a few tens of nanometers in diameter that also form during nanowire growth.

Fig. 5.1(b) shows the temperature dependence of the resistivity, ρ_{xx}(T) of a typical RuO_2 nanowire, that was patterned as a Hall Bar of width around 650 nm, thickness around 100 nm and with a distance between the contacts around 2.6 μm. The 300 K resistivity ρ_{300} is 71 $\mu\Omega$.cm while the low-temperature (10 K) specific resistance ρ_{10} is 13.5 $\mu\Omega$.cm. This gives a residual-resistivity ratio (RRR, the ratio between ρ_{300} and ρ_{10}) of around 5.3. The wire has positive temperature coefficient of resistance at all temperatures including at low temperatures, as seen in inset of Fig. 5.1(b), which suggests very little or no grain boundary scattering of electron and a high crystal quality of the RuO_2 nanowires.

We further characterized RuO_2 wires through Hall measurements at different temperatures. Fig. 5.1(d) shows measurements of the Hall resistivity as a function of an out-of-plane magnetic field for different temperatures in a range from 300 K to 10 K. The data are represented as ρ_{xy} as function of magnetic field, with $\rho_{xy} = \frac{V_{xy}t}{I}$. Here, V_{xy} is the transverse voltage, I is the measurement current, and t is the thickness of the wire. $\rho_{xy}(\mu_0 H)$ is linear for all the measured temperatures and

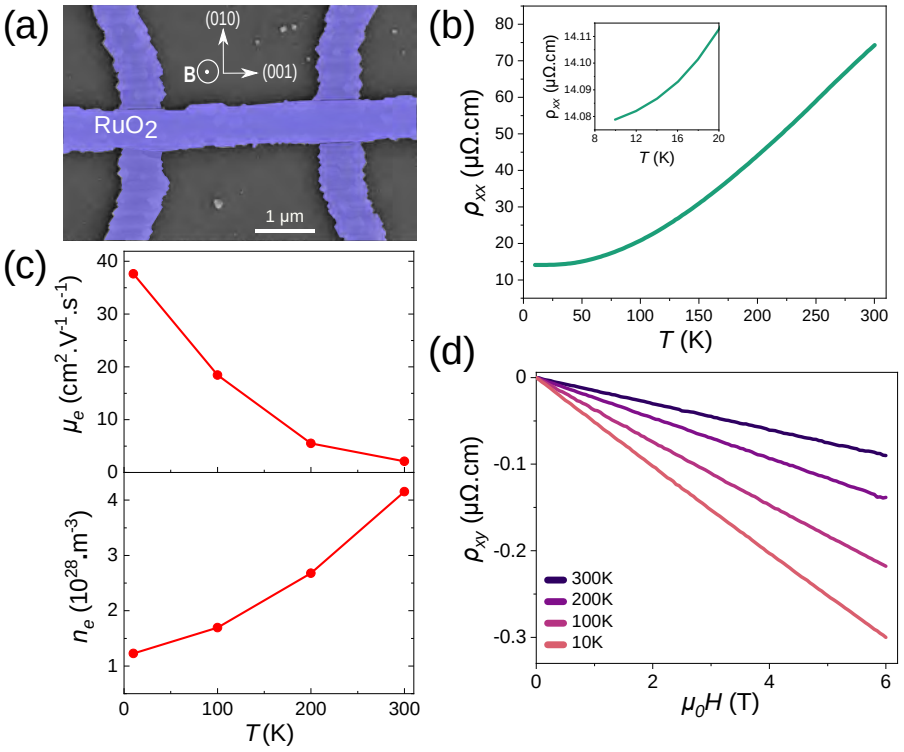

Figure 5.1: (a) SEM image (false color) of a RuO_2 nanowire grown using Selective Area Growth. The magnetic field B is applied out of the plane for Hall characterization measurements. (b) Longitudinal resistivity as a function of temperature for a RuO_2 nanowire with dimensions of approximately 2.6 μm in length between contacts and 650 nm in width; inset shows the positive temperature coefficient of resistance at lower temperature indicating that high crystal quality. (c) mobility (μ_e) (top) and charge carrier density (n_e) (bottom) at different temperature indicating that the behavior is unlike normal metal where n_e stays constant with temperature (d) Hall resistivity as a function of applied field measured at various temperature between 10 K to 300 K.

the field with a slope that corresponds to electron-like charge carriers. Carrier density (n) and mobility (μ_e) follow in a one-band model from $\rho_{xy} = -\frac{\mu_0 H}{e \cdot n}$ and $\mu_e = \frac{\sigma_{xx}}{e \cdot n}$ where, σ_{xx} is $1/\rho_{xx}$. Their values and temperature dependence are plotted in Fig. 5.1c. It is interesting to note that charge carrier density decreases with temperature and is nearly 4 times lower at 10 K than at 300 K.

5.3. Methods

Junction fabrication: To fabricate the lateral JJs (Fig. 2a), the initial step involved using SA technique to grow RuO_2 nanowires with dimensions of approximately

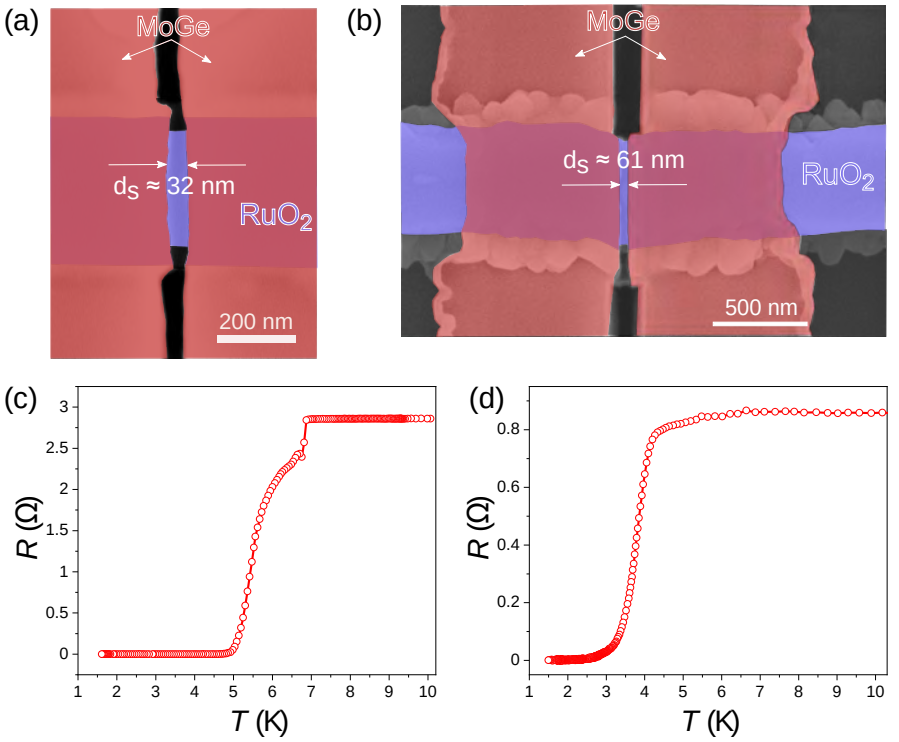

Figure 5.2: SEM image (false color) of the fabricated Josephson junctions (JJ) comprising RuO_2 nanowire (in blue) and MoGe as the superconducting contacts (in peach) that are laterally edge to edge separated by (a) 32 nm for J1 and (b) and 61 nm for J2. (c), (d) Resistance vs temperature plot between (10 to 1.5) K showing the transition temperature (T_c) for the junctions (c) J1 and (d) J2. We have taken T_c as the temperature at which the resistance has decreased to 50% of the normal resistance value, which for J1 is 5.5 K and for J2 is 3.8 K.

30 μm in length and 250 nm in width, along the [001] direction. The contacts were subsequently patterned on top of the RuO_2 nanowire using e-beam lithography. 100 nm of MoGe sputter deposited at a pressure of 5×10^{-3} mbar, which was followed by a lift-off process. Finally, the weak link was created using Focused Ion Beam (FIB) etching. In this way, three different junction devices were fabricated, with an edge-to-edge gap between the MoGe contacts of 32 nm (J1), 61 nm (J2) and 105 nm (J3). Here, a caveat is needed. In particular the 32 nm trench is both hard to make uniform, and proved not easy to measure in the SEM. The estimate should rather be 27 nm - 38 nm. Moreover, the cut for this sample also made the wire locally smaller. For the wider bridges, fewer issues were experienced. Also, generally, the cuts were quite deep, meaning that the RuO_2 bridge was thinner than it nominal value. Still, some clear conclusions can be drawn, as we will discuss below.

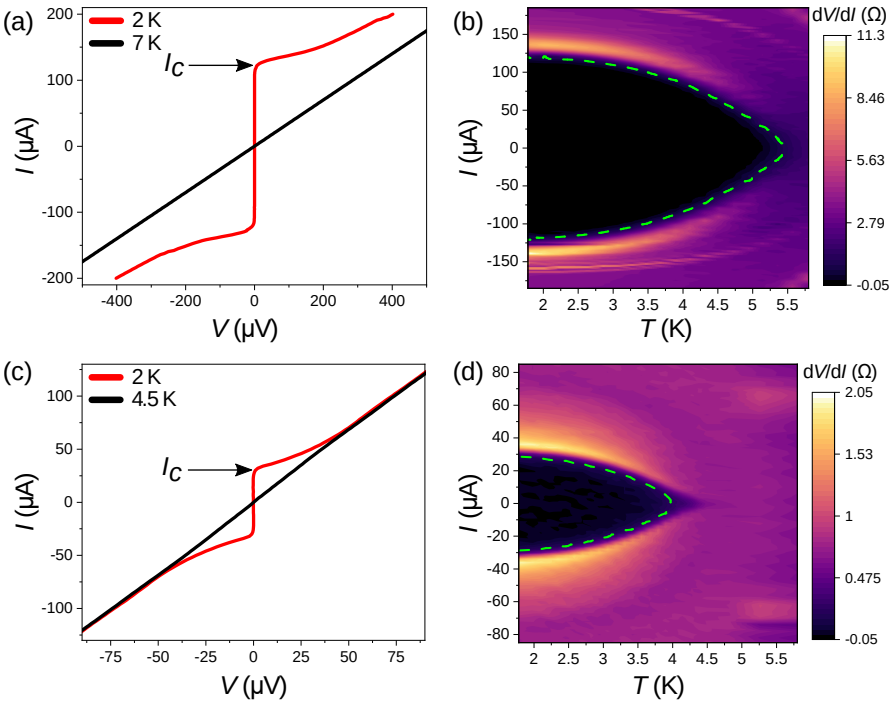

Figure 5.3: (a) and (c) I-V measurements taken above (black) and below (red) superconducting transition of J1 and J2 devices respectively. (b) and (d) shows I-dV/dI plot measured over different temperatures in steps of (b) 200 mK and (d) 100 mK. The dotted green line is the associated critical current I_c as a function of temperature T at dV/dI of 0.42 for both J1 and J2.

Device	T (K)	I_c (μA)	R_n (Ω)	d_s (nm)	V_c (μV)
J1 (E5-2.1)	1.8	121	2.85	32 ±6	345
J2 (H4-1.1)	1.8	29.3	0.86	61	25.2
J3 (E5-1.2)	1.5	0	3.11	105	0

Table 5.1: Critical current at measured temperature, normal resistance, junction length and the corresponding critical voltage of three Josephson junction devices based on RuO_2 nanowires.

Fig. 5.2(a), (b) shows the SEM images (false color) of the devices J1 and J2 respectively, consisting of RuO_2 nanowire (blue) and MoGe electrodes (peach) on top of RuO_2. Fig. 5.2(c), (d) give their corresponding resistive transitions. The critical temperature of the MoGe is about 7 K, and visible as a tiny step (in J1), or a deviation from constant resistance (J2). A clear drop in resistance due to the contacts going superconducting is not expected, since this is a 4-point measurement. The normal state resistance in both cases (about 3 Ω for J1, 0.8 Ω for J2) is quite different, mainly due to the difference in trench depth. The transition temperature T_c, defined by

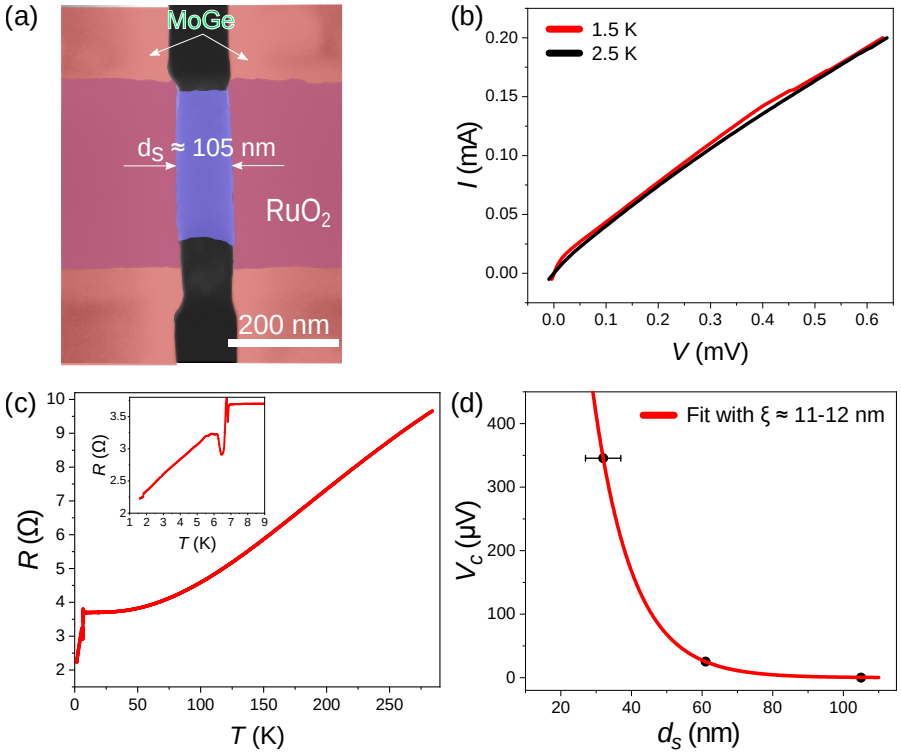

Figure 5.4: (a) SEM image of the device J3 where d_s = 105 nm. (b) I-V characteristics measured at 2.5 K (black) and 1.5 K(red) at zero-field shows very small non-linearity. (c) R(T) behavior of J3 measured from 280 K down to 1.5 K. Inset shows the R-T for temperature between 9 K to 1.5 K. A sharp drop in resistance is measured around 6.8 K signalling the superconducting transition MoGe. By 1.5 K, the normal state resistance of the wire has dropped by 41% which is a clear signature of partial proximization of the junction. (d) $V_c = I_c R_n$ as a function of d_s for the 3 JJ devices. The red curve is the fitted exponential decay function which gives coherence length (ξ) in RuO_2 of around 12 nm.

the midpoint of the resistive transition, was also different, about 5.5 K for J1, and about 4 K for J2. These devices, with the smallest gaps, showed clear Josephson junction behavior. Device J3 with a 105 nm gap proximized only partially, meaning that zero resistance was not reached till 1.5 K. Table 5.1 summarizes the basic device parameters.

5.4. Results and Discussion

We measured the zero-field current(I)-voltage(V) behavior of the two JJs J1 and J2 as function of temperature. Typical IV characteristics are shown in Fig. 5.3(a),

(c) while Fig. 5.3(b), (e) shows the color plot of I versus the derivative-dV/dI. We extracted the $I_c(T)$ from the onset of a change in the derivative, shown by the dotted line (green) in the Fig. 5.3(b), (e). We observed that the temperature of the onset of supercurrent coincides with the temperature of the midpoint of the resistive transition. At the lowest temperatures, I_c has become nearly constant. These low-temperature values show a strong decrease of I_c with increasing gap, dropping from 121 μA in J1 to 30 μA in J2.

We further fabricated and measured device J3 with a gap d_s = 105 nm, which did not reach zero resistance. Fig. 5.4a shows the R(T) measurement from 300 K down to 1.5 K. We observe that the resistance becomes constant below 10 K, with a value of 3.7 Ω around 8K. When the MoGe electrodes become superconducting at 6.8 K the resistance starts to decrease again (after a small dip-peak excursion) but does not reach 0 Ω. This behavior indicates that the RuO_2 wire did not proximize completely over the whole length of the junction. In contrast, a reduction of around 41% in resistance from the normal state resistance is seen when the temperature is lowered to 1.5 K. This reduction translates to a proximity length of about 20 nm extending from each contact.

Using the three JJ devices parameters, the coherence length ξ of the supercurrents can be estimated. For this we use the decay of the coupling strength, given by the product $I_cR_N = V_c$. This ensures that the actual dimensions of the bridge, as given by R_N, are taken into account correctly. We fit $V_c(d_s)$ using an exponential decay function $V_c(d_s) \propto exp(-\frac{d_s}{\xi})$. For our devices we estimate, $\xi \approx 12$ nm as shown in the Fig. 5.4(c). This matches quite well with the proximity length that we estimated to be induced in the longer junction J3. We also note that the order of magnitude reflects the size of the Ru-moment: in the collinear AF magnet IrMn, with a Mn moment of 3 μ_B, the coherence length was estimated 3 - 5 nm[14] (even quite large for such moments, possibly because it is an AF); in weak ferromagnets such as $Pd_{1-x}Ni_x$ or $Cu_{1-x}Ni_x$, it is found that the superconducting decay length (the dirty-limit coherence length ξ_F) is of the order of 5 nm for magnetic moments in the range 0.1 - 0.2 μ_B [24–26]. Finding 12 nm for an AF with moments of 0.05 μ_B appears quite reasonable. We further measured our devices in the magnetic field and observed a Fraunhofer-like damped oscillatory response of I_c, as expected for a Josephson Junction. Fig. 5.5(a), (b) shows the color plot of the magnetic field interference pattern $I_c(\mu_0 H)$. In the case of J1, we measured at a temperature of 2.5 K while the field was varied between -130 mT to 130 mT. For J2, we measured at 1.5 K while the field was varied from 0 to 185 mT. For J2 in particular, the first and second minimum, and thereby the width of the lobes, can be estimated fairly well to be about 45 mT. To interpret these data, we have to consider the following. In conventional Josephson junctions that are formed by a barrier sandwiched between two superconducting

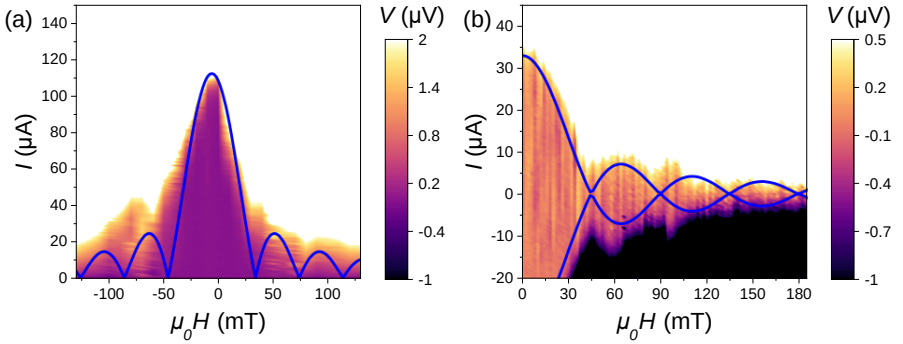

Figure 5.5: I-V characteristics of the JJ devices (a) J1 at 2.5 K and (b) J2 1.2 K when applying out of plane magnetic field. The blue curve is the simulated Fraunhofer pattern for our devices dimensions, representing the relation between critical current I_c and the applied magnetic flux.

electrodes, sometimes called overlap-type junctions, the (Fraunhofer) interference patterns can be described by

$$I_c(\mu_0 H) = I_c^{max} \left| \frac{\sin(\frac{\pi\Phi}{\Phi_0})}{\frac{\pi\Phi}{\Phi_0}} \right| \tag{5.1}$$

where I_c^{max} is the maximum critical current of the junction at zero field and $\Phi_0 = \frac{h}{2e}$ is the magnetic flux quantum (fluxoid). The magnetic flux ϕ is given by

$$\Phi = \mu_0 H A_{flux}^{eff}\,. \tag{5.2}$$

Here, $\mu_0 H$ is the external applied magnetic field *in* the interface plane of the junction, and A_{flux}^{eff} is the effective area of the junction given by $(2\lambda_L + d_s)\,w$, with λ_L the London penetration depth and w the width of the junction device. Using this overlap-junction description for our planar junctions, but with the applied field now perpendicular to the junction plane, we note that zero values for I_c are reached when $\Phi = n\Phi_0$ (with n an integer), so the width of the lobes $\Delta(\mu_0 H) = \Delta B$ is given by $\Delta B = \Phi_0 / A_{flux}^{eff}$. Using the lobe width of 45 mT, this would lead to $A_{flux}^{eff} \approx 0.045\ \mu\text{m}^2$. However, when calculating A_{flux}^{eff} from the values of w ≈ 250 nm (width of the devices), and $\lambda_L \approx 580$ nm[27, 28], we obtain $A_{flux}^{eff} \approx 0.32\ \mu m^2$, which is a very different and also unrealistic number. For completeness, we display a simulated Fraunhofer pattern for the measured lobe width in Fig. 5.5(a), (b) (blue curve).

The reason for erroneous calculation of A_{flux}^{eff} is that the junction physics becomes different when the thickness of the superconducting electrodes is less than their London penetration depth, as is often the case for planar junctions. Additionally, when the junction width w becomes smaller than the Josephson penetration

length ℓ_J given by $\Phi_0/(4\pi\mu_0\lambda_L^2 j_c(0)$, with j_c being the (presumed homogeneous) critical current density of the junction. In this scenario, as has been discussed in numerous studies, the electrodynamics becomes non-local, and $I_c(B)$ becomes independent of λ_L and is solely determined by the geometry of the device [29–33]. In our junctions, the thickness d of the MoGe layer (100 nm) is smaller than the bulk London penetration depth (580 nm). Consequently, the relevant penetration depth for the electrodes is given by the Pearl length $\Lambda = 2\lambda_L^2/d$. The calculated Λ is $\approx$ 6.7μm, which is significantly larger than the size of electrodes. Using the measured $I_c(0)$ of about 0.1 mA through a cross-section of w = 250 nm and thickness t = 100 nm, we estimate ℓ_J to be $\approx$ 97 nm. The junction width is actually somewhat lager than this, but it was discussed in Ref.[32] that non-local electrodynamics still apply. The simple answer for the lobe width in the interference pattern is that $\Delta B = 1.84\Phi_0/w^2$ [31, 33].The lobe width ΔB = 45 nm then corresponds to a junction width of 290 nm, quite close to the actual number. We conclude that, under a perpendicular magnetic field, our junctions show the behavior expected for planar junctions.

5.5. Summary

In summary, we have grown high quality RuO_2 nanowires using the Selective Area (SA) growth on a TiO_2 substrate and used these to fabricate planar Josephson junctions with the RuO_2 wire as a weak link. We find these links not to behave as a normal metal; rather, the pair breaking effects are similar to what is found in weak ferromagnets such as CuNi and PdNi. The estimated coherence length of the weak link is about 12 nm. Moreover, the junctions behave as expected for planar junctions of such dimensions under the application of a magnetic field.

5.6. Appendix

5.6.1. A shorted junction

We also measured a device where voltage probes are shorted. Fig. 5.6(a) shows that at the device becomes superconducting below the T_c of MoGe. The response of the device in magnetic field as expected shows the current hardly varies. This is in sharp contrast to the Fraunhofer-like pattern of junctions in Fig. 5.5.

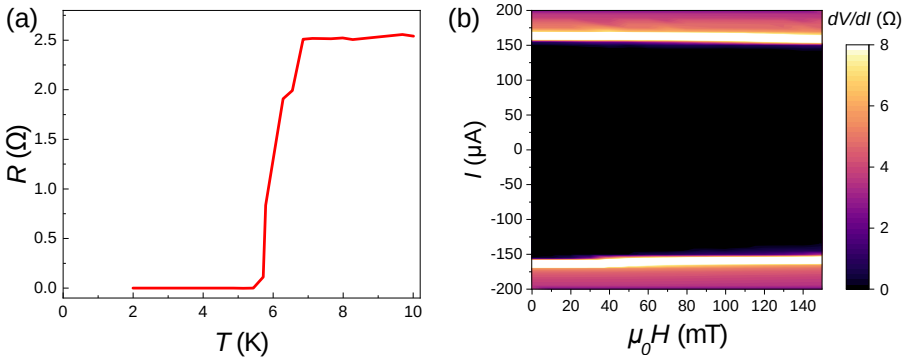

Figure 5.6: (a) R(T) between 10 K to 2 K of a shorted -junction device. The device becomes superconducting below 6K. (b) Color plot of I($\mu_0 H$)of a shorted-junction device measured at 2 K. Field is applied out of plane to the device interface and varied from 0 to 150 mT. As expected current (I) stays almost constant under the whole range of field.

5.6.2. Closeup of a RuO_2 nanowire

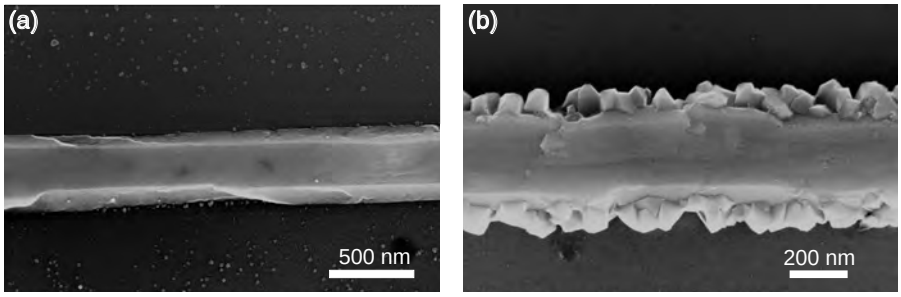

Figure 5.7: High resolution close up SEM images of two RuO_2 nanowires

Fig. 5.7 shows a high resolution scanning eletron micrograph of two epitaxially grown RuO_2 nanowires of similar width of around 250 nm. In both cases, well defined crystal facets can be seen clearly. In (a) the width of the wire is completely inside the trench. There are very small and thin crystals on SiOx but away from the trench. However, for (b) thin crystal shards are attached to the side along the length of the wire. A probable explanation is that RuO_2 is known to grow on SiOx surface. The growth on SiOx is at a much slower rate. At the edge of the trench on both sides, these small crystals merged with the wire to give the above irregular growth.

References

[1] Sun, Y., Zhang, Y., Liu, C.-X., Felser, C. & Yan, B. Dirac nodal lines and induced spin hall effect in metallic rutile oxides. Phys. Rev. B **95**, 235104 (2017). URL https://link.aps.org/doi/10.1103/PhysRevB.95.235104.

[2] Wang, R. et al. Nodal line fermions in magnetic oxides. Phys. Rev. B **97**, 241111 (2018). URL https://link.aps.org/doi/10.1103/PhysRevB.97.241111.

[3] Dismukes, J. P., Martin, D. F., Ekstrom, L., Wang, C. C. & Coutts, M. D. Ferromagnetic chromium dioxide for magnetic tape. Ind. Eng. Chem. Prod. Res. Dev. **10**, 319 (1971). URL https://doi.org/10.1021/i360039a013.

[4] Keizer, R. S. et al. A spin triplet supercurrent through the half-metallic ferromagnet CrO_2. Nature **439**, 825–827 (2006). URL http://dx.doi.org/10.1038/nature04499.

[5] Anwar, M. S., Veldhorst, M., Brinkman, A. & Aarts, J. Long range supercurrents in ferromagnetic CrO_2 using a multilayer contact structure. Appl. Phys. Lett. **100**, 052602 (2012). URL http://aip.scitation.org/doi/10.1063/1.3681138.

[6] Singh, A., Jansen, C., Lahabi, K. & Aarts, J. High-Quality CrO_2 Nanowires for Dissipation-less Spintronics. Phys. Rev. X **6**, 041012 (2016). URL https://link.aps.org/doi/10.1103/PhysRevX.6.041012.

[7] Fujiwara, K. et al. 5d iridium oxide as a material for spin-current detection. Nature Comm. **4**, 2893 (2013). URL http://dx.doi.org/10.1038/ncomms3893.

[8] Qiu, Z., Hou, D., Kikkawa, T., i Uchida, K. & Saitoh, E. All-oxide spin seebeck effects. Appl. Phys. Express **8**, 083001 (2015). URL http://dx.doi.org/10.7567/APEX.8.083001.

[9] Berlijn, T. et al. Itinerant antiferromagnetism in RuO_2. Phys. Rev. Lett. **118**, 077201 (2017). URL https://doi.org/10.1103/PhysRevLett.118.077201.

[10] Zhu, Z. H. et al. Anomalous antiferromagnetism in metallic RuO_2 determined by resonant x-ray scattering. Phys. Rev. Lett. **122**, 017202 (2019). URL https://link.aps.org/doi/10.1103/PhysRevLett.122.017202.

[11] Šmejkal, L., González-Hernández, R., Jungwirth, T. & Sinova, J. Crystal time-reversal symmetry breaking and spontaneous hall effect in collinear antiferromagnets. Science Advances **6**, eaaz8809 (2020). URL https://www.science.

org/doi/abs/10.1126/sciadv.aaz8809. https://www.science.org/doi/pdf/10.1126/sciadv.aaz8809.

[12] Feng, Z. et al. An anomalous hall effect in altermagnetic ruthenium dioxide. Nature Electronics **5**, 735–743 (2022). URL https://doi.org/10.1038/s41928-022-00866-z.

[13] Uchida, M., Nomoto, T., Musashi, M., Arita, R. & Kawasaki, M. Superconductivity in uniquely strained RuO_2 films. Phys. Rev. Lett. **125**, 147001 (2020). URL https://doi.org/10.1103/PhysRevLett.125.147001.

[14] Jeon, K.-R. et al. Long-range supercurrents through a chiral non-collinear antiferromagnet in lateral josephson junctions. Nature Materials **20**, 1358–1363 (2021). URL https://doi.org/10.1038/s41563-021-01061-9.

[15] Selte, K., Kjekshus, A., Andresen, A. F. & Pearson, W. B. A neutron diffraction study of magnetic ordering in the irmn phase. Acta Chem. Scand. **22**, 3039 (1968).

[16] Ahn, K.-H., Hariki, A., Lee, K.-W. & Kuneš, J. Antiferromagnetism in RuO_2 as d-wave pomeranchuk instability. Phys. Rev. B **99**, 184432 (2019). URL https://link.aps.org/doi/10.1103/PhysRevB.99.184432.

[17] Hayami, S., Yanagi, Y. & Kusunose, H. Momentum-dependent spin splitting by collinear antiferromagnetic ordering. Journal of the Physical Society of Japan **88**, 123702 (2019). URL https://doi.org/10.7566/JPSJ.88.123702. https://doi.org/10.7566/JPSJ.88.123702.

[18] Šmejkal, L., Sinova, J. & Jungwirth, T. Beyond conventional ferromagnetism and antiferromagnetism: A phase with nonrelativistic spin and crystal rotation symmetry. Phys. Rev. X **12**, 031042 (2022). URL https://link.aps.org/doi/10.1103/PhysRevX.12.031042.

[19] Bai, H. et al. Observation of spin splitting torque in a collinear antiferromagnet ruo_2. Phys. Rev. Lett. **128**, 197202 (2022). URL https://link.aps.org/doi/10.1103/PhysRevLett.128.197202.

[20] Bose, A. et al. Tilted spin current generated by the collinear antiferromagnet ruthenium dioxide. Nature Electronics **5**, 267–274 (2022). URL https://doi.org/10.1038/s41928-022-00744-8.

[21] Karube, S. et al. Observation of spin-splitter torque in collinear antiferromagnetic RuO_2. Phys. Rev. Lett. **129**, 137201 (2022). URL https://link.aps.org/doi/10.1103/PhysRevLett.129.137201.

[22] Prateek, K. et al. Magnetotransport properties of CrO_2 nanowires fabricated by selective area growth. Journal of Physics and Chemistry of Solids **178**, 111350 (2023). URL https://www.sciencedirect.com/science/article/pii/S0022369723001403.

[23] Si, J. & Desu, S. B. RuO_2 films by metal-organic chemical vapor deposition. Journal of Materials Research **8**, 2644–2648 (1993). URL https://doi.org/10.1557/JMR.1993.2644.

[24] Cirillo, C. et al. Superconducting proximity effect and interface transparency in nb/pdni bilayers. Phys. Rev. B **72**, 144511 (2005). URL https://link.aps.org/doi/10.1103/PhysRevB.72.144511.

[25] Rusanov, A., Boogaard, R., Hesselberth, M., Sellier, H. & Aarts, J. Inhomogeneous superconductivity induced in a weak ferromagnet. Physica C **369**, 300 (2002).

[26] Oboznov, V. A., Bol'ginov, V. V., Feofanov, A. K., Ryazanov, V. V. & Buzdin, A. I. Thickness dependence of the josephson ground states of superconductor-ferromagnet-superconductor junctions. Phys. Rev. B **96**, 197003 (2006). URL https://link.aps.org/doi/10.1103/PhysRevLett.96.197003.

[27] Motta, M. et al. Controllable morphology of flux avalanches in microstructured superconductors. Phys. Rev. B **89**, 134508 (2014). URL https://link.aps.org/doi/10.1103/PhysRevB.89.134508.

[28] Draskovic, J. et al. Measuring the superconducting coherence length in thin films using a two-coil experiment. Phys. Rev. B **88**, 134516 (2013). URL https://link.aps.org/doi/10.1103/PhysRevB.88.134516.

[29] Kogan, V. G., Dobrovitski, V. V., Clem, J. R., Matawari, Y. & Mints, R. G. Josephson junction in a thin film. Phys. Rev. B **63**, 144501 (2001). URL https://link.aps.org/doi/10.1103/PhysRevB.63.144501.

[30] Moshe, M., Kogan, V. G. & Mints, R. G. Edge-type josephson junctions in narrow thin-film strips. Phys. Rev. B **78**, 020510R (2008). URL https://link.aps.org/doi/10.1103/PhysRevB.78.020510.

[31] Clem, J. R. Josephson junctions in thin and narrow rectangular superconducting strips. Phys. Rev. B **81**, 144515 (2010). URL https://link.aps.org/doi/10.1103/PhysRevB.81.144515.

[32] Boris, A. A. et al. Evidence for nonlocal electrodynamics in planar josephson junctions. Phys. Rev. Lett. **111**, 117002 (2013). URL https://link.aps.org/doi/10.1103/PhysRevLett.111.117002.

[33] Fermin, R., de Wit, B. & Aarts, J. Beyond the effective length: How to analyze magnetic interference patterns of thin-film planar josephson junctions with finite lateral dimensions. Phys. Rev. B **107**, 064502 (2023). URL https://link.aps.org/doi/10.1103/PhysRevB.107.064502.